Available online at www.sciencedirect.com

jmr&t Journal of Materials Research and Technology

journal homepage: www.elsevier.com/locate/jmrt

Original Article

Simulation of phase evolution in a Zr-based glass forming alloy during multiple laser remelting

Johan Lindwall [a,*], *Anders Ericsson* [b], *Jithin James Marattukalam* [c], *Carl-Johan Hassila* [e], *Dennis Karlsson* [d,g], *Martin Sahlberg* [d], *Martin Fisk* [b,f], *Andreas Lundbäck* [a]

[a] *Department of Engineering Sciences and Mathematics, Luleå University of Technology, SE-971 87, Luleå, Sweden*
[b] *Division of Solid Mechanics, Lund University, Box 118, SE-221 00, Lund, Sweden*
[c] *Department of Physics and Astronomy, Uppsala University, Box 538, SE-751 21, Uppsala, Sweden*
[d] *Department of Chemistry - Ångström Laboratory, Uppsala University, Box 538, SE-751 21, Uppsala, Sweden*
[e] *Department of Materials Science and Engineering, Uppsala University, Box 538, SE-751 21 Uppsala, Sweden*
[f] *Materials Science and Applied Mathematics, Malmö University, SE-205 06, Malmö, Sweden*
[g] *Sandvik Materials Technology, SE-811 81, Sandviken, Sweden*

ARTICLE INFO

Article history:
Received 18 August 2021
Accepted 11 December 2021
Available online 17 December 2021

Keywords:
Simulation of laser-based powder bed fusion
Metallic glass
Phase transformation modelling
Classical nucleation and growth theory

ABSTRACT

Additive manufacturing by laser-based powder bed fusion is a promising technique for bulk metallic glass production. But, reheating by deposition of subsequent layers may cause local crystallisation of the alloy. To investigate the crystalline phase evolution during laser scanning of a Zr-based metallic glass-forming alloy, a simulation strategy based on the finite element method and the classical nucleation theory has been developed and compared with experimental results from multiple laser remelting of a single-track. Multiple laser remelting of a single-track demonstrates the crystallisation behaviour by the influence of thermal history in the reheated material. Scanning electron microscopy and transmission electron microscopy reveals the crystalline phase evolution in the heat affected zone after each laser scan. A trend can be observed where repeated remelting results in an increased crystalline volume fraction with larger crystals in the heat affected zone, both in simulation and experiment. A gradient of cluster number density and mean radius can also be predicted by the model, with good correlation to the experiments. Prediction of crystallisation, as presented in this work, can be a useful tool to aid the development of process parameters during additive manufacturing for bulk metallic glass formation.

* Corresponding author.
E-mail address: Johan.Lindwall@ltu.se (J. Lindwall).

https://doi.org/10.1016/j.jmrt.2021.12.056

1. Introduction

Metallic glass possesses desirable properties for many mechanical applications because of its amorphous structure. The amorphous structure enables for high elastic strain limits, high yield stresses, exceptional wear and corrosion resistance [1]. Manufacturing of bulk metallic glass (BMG) by traditional casting techniques are generally restricted by the cooling rate required to bypass crystallisation. With additive manufacturing by laser-based powder bed fusion (PBF-LB) it is possible to obtain cooling rates far greater (up to 10^8 K/s) than the typical critical cooling rate for bulk glass forming alloys (10^1–10^3 K/s [1]). However, reheating of subsequent deposited layers during printing can cause crystallisation in the amorphous phase, primarily in the heat affected zone (HAZ) as discussed in the reviews by Williams and Lavery [2] and Liu et al. [3].

It has been demonstrated in several studies that the PBF-LB process parameters have a significant impact on the resulting relative density and phase structure in the manufactured material. A low energy density input can be beneficial for suppressing the formation of a crystalline structure, but it can also result in lack of fusion [4,5]. Increasing the laser energy on the other hand, may lead to crystallisation [6]. It was clearly shown in experimental studies by Yang et al. [7] and Zhang et al. [8] that formation of crystals in the HAZ is more likely for an increasing number of reheating cycles. Each reheating cycle induces more nuclei and the possibility of growth of already existing clusters. The HAZ will always be present around the fusion zone and reheating from the subsequent layers or adjacent hatches during PBF-LB results in a cyclic temperature history over a wide temperature range that affects crystallisation [2,9]. In order to predict the probability for crystallisation of the BMG, it would therefore be advantageous to simulate nucleation and growth of crystals during the thermal history of PBF-LB based on the process parameters.

The cyclic temperature history at high heating and cooling rates add challenges in terms of modelling of crystallisation. It requires that the rate of formation through nucleation and/or growth has to be treated with appropriate temporal resolution as they are well known to possess peak rates at different temperatures [1,10–12]. Since the peak nucleation rate occurs at a lower temperature than the peak growth rate, nuclei that form during one cycle may not grow until the material has been heated. Furthermore, computation of the thermal field and the crystallisation process are generally performed at different spatial and temporal resolutions, which makes direct coupling difficult and imposes computational restrictions on the underlying phase transformation model. The classical nucleation and growth theory (CNT) addresses the aforementioned issues by treating the rate of crystalline formation through nucleation and growth by solving them separately. The equations are computationally efficient and can be solved in sub-steps within a finite element (FE) software describing the evolution of the thermal field [13]. Shen et al. [14] presented a model based on CNT to calculate the crystalline phase evolution within the HAZ of a Zr-based alloy. The model applies the temperature history achieved by thermal simulation of laser processing on a single string with varying scanning speed to investigate the crystallisation in discrete location in the HAZ. Ericsson et al. [15] modelled the crystalline phase formation of another Zr-based BMG during a PBF-LB thermal history by numerically solving the governing equations for nucleation within the classical nucleation theory. It was demonstrated, based on a selected temperature history in the PBF-LB process, that transient nucleation effects can be significant due to the high heating and cooling rates. Such simulations can increase the understanding of the crystalline phase formation at the selected locations based on the temperature history. By coupling the phase transformation model to the thermal simulation it becomes possible to compute the evolution of crystalline precipitates in a three-dimensional domain in the FE-software.

This study presents a modelling strategy based on the FE-method to simulate the crystalline phase evolution in the glass forming alloy $Zr_{59.3}Cu_{28.8}Al_{10.4}Nb_{1.5}$ at.%, also known as AMZ4 [16], during multiple remelting of a single laser scan. For this, a phase transformation model by steady-state nucleation has been implemented in a thermal FE-model and solved for each time step and all integration points in a control volume. A de-coupled model for transient nucleation has also been used to compute the phase evolution at selected discrete locations. The transient model are much more time consuming to solve, but expects to give more accurate results. The simulations are compared with experimental results from multiple laser remelting on an AMZ4 substrate produced by PBF-LB. Simulations may be a useful tool to understand the evolution of crystalline phases by the influence of laser scanning parameters and the influence of temperature history caused by successive reheating of the already processed material.

2. Experimental procedure

The starting point for the modelling is BMG substrates produced to be XRD-amorphous. To investigate the influence of thermal history during manufacturing, a multiple laser remelting of a single-track experiment has been developed. The thermal conductivity of the AMZ4 amorphous alloy has been measured in this work.

2.1. *Bulk metallic glass substrate*

Rectangular AMZ4 plates with dimensions 22 mm in length, 11 mm in width and 2 mm in thickness were manufactured on a titanium build plate using an EOS M100 (EOS GmBH, Germany), a PBF-LB system equipped with a continuous ytterbium fibre laser with wavelength between 900 and 1200 nm [17]. The powders used for printing was produced by Heraeus, GmbH and was X-ray amorphous, further details can be found in [5]. The motion of laser beam was controlled by an optical scanner with a constant speed of 2000 mm/s at the focal plane. Samples were produced using a rotating scan strategy where the scanning direction was rotated 67° for each layer. Furthermore, a re-melting approach was used, where each layer was scanned twice. The second scan for each layer was scanned at a 90° angle relative to the first scan. The laser beam diameter was 40 μm and the power was set to 75 W. The layer thickness was 20 μm and the hatch spacing 100 μm. The process parameters were developed to result in minimum

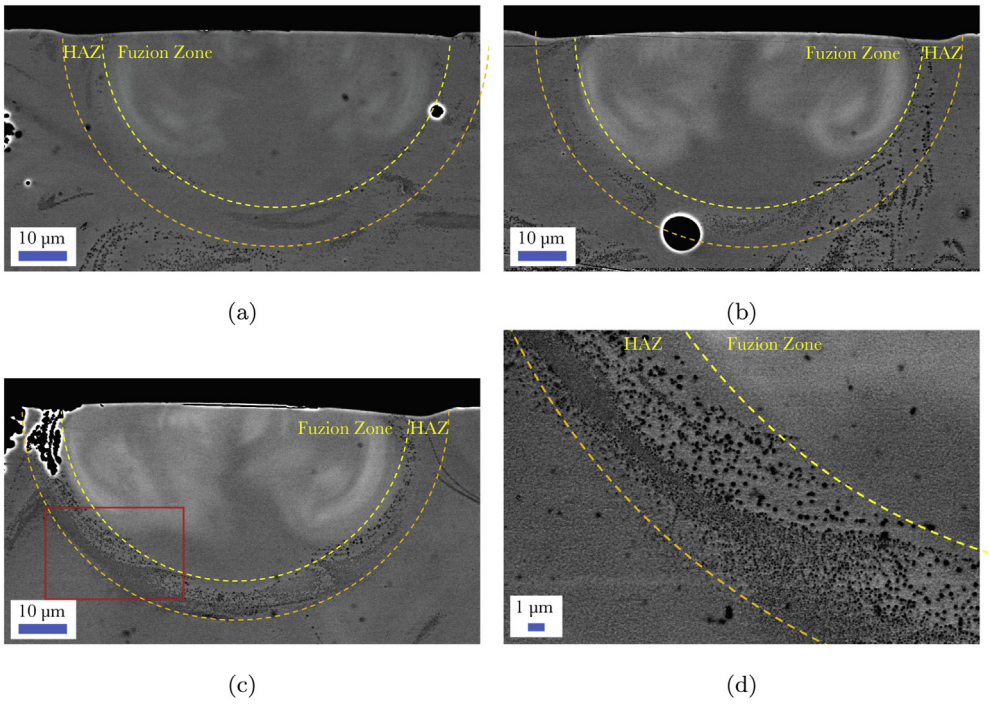

Fig. 1 – SEM BSD imaging of cross section perpendicular to the laser track direction after one to three passes (a–c). The highlighted area of the HAZ after the third scan is also magnified in (d). Gray scale indicates the material density from light (dark) to heavy (bright).

porosity and crystallisation in the produced material [5]. The produced samples remained XRD-amorphous with the used settings. However, nano-sized crystals as a consequence of the overlapping HAZ during the PBF-LB processing, might be expected. The processing were performed in an argon-shielded build chamber. The oxygen content reported of the printed AMZ4 samples used in this study is approximately 1 at % (0.2 wt%), determined using inert gas fusion method [5].

2.2. *Single-track remelting*

The as-printed plates were cut from the substrate and polished using a series of SiC emery papers followed by 9 and 3 μm diamond suspension to obtain a mirror like finish. Single tracks were scanned on the plates with consecutive melting up to three times in order to impose formation of crystals in the HAZ. Each track was scanned a number of times proportional to its track position (e.g. track number two was scanned twice). The length of each track was 20 mm and they were separated approximately 2–3 mm. The scanning speed was 2000 mm/s and the time between each consecutive scan was long enough to avoid accumulation of thermal energy in the material.

The laser scanned plates were cut perpendicular to the scanning direction, polished with the same aforementioned procedure and analysed using scanning electron microscopy (SEM) to obtain information of the fused zone (FZ) geometry and crystallinity in the HAZ. SEM was performed on as Zeiss merlin equipped with a back scattered electron (BSD) detector, an acceleration voltage of 20 kV was used at a working distance of 7.8 mm.

The microstructure in HAZ were further investigated using transmission electron microscopy (TEM) analysis carried out in TEM mode using a FEI Titan Themis instrument operated at 200 kV acceleration voltage. The diffraction patterns and high-resolution images were evaluated by the CrysTBox toolbox [18]. The TEM lamella was prepared using the *in-situ* lift-out technique in a Zeiss Crossbeam 550 focused ion beam (FIB). The surface was coated with platinum to protect from ion damage during preparation, and a final polishing step using 5 keV ions were employed to minimize ion damage.

2.3. *Measurement of thermal conductivity*

For simulation of the temperature field, the thermal conductivity and heat capacity of PBF-LB manufactured AMZ4 was measured using the transient plane source (HotDisk) method using a TPS2500 with a sensor type 5465 by the Swedish research institute RISE. The sensor was squeezed between two smooth XRD-amorphous discs (printed and polished) with a diameter of 20.0 mm and a thickness of 10.02–9.98 mm in an air sealed tube furnace. Three different measurements were performed: room temperature (RT), 200 and 299 °C when the temperature stabilized in the material.

3. Experimental analysis of single-track remelting

The SEM images shown in Fig. 1 reveal the evolution of crystals in the HAZ during the single laser remelting experiments

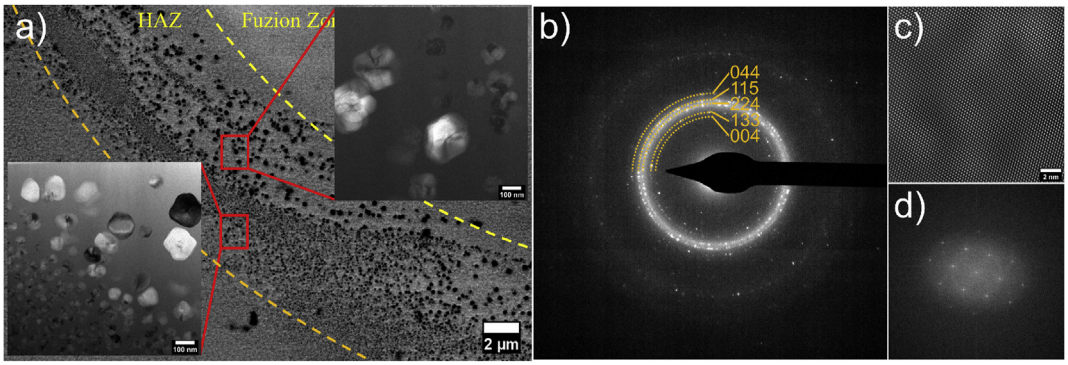

Fig. 2 – a) SEM image of the HAZ, indicating two regions for further analysis by TEM (bright field images shown in the insets). Bright field image in the outer region of the HAZ reviles varying crystal sizes, from around 30 to 150 nm in diameter and the corresponding electron diffraction pattern indexed with the Cu_2Zr_4O phase is shown in b). A Fourier filtered high resolution (HRTEM) image oriented in the [101] zone axis of the Cu_2Zr_4O phase is shown in c) with the Fourier transform shown in d).

in a cross-section perpendicular to the scanning direction. Some localized crystallinity and porosity were observed in the as-printed AMZ4 plates as a result of the manufacturing process. Hence, it can be assumed that formation of crystals in the HAZ during the experiments are assisted by the already existing nuclei. It should be noted that the crystallography has been investigated in detail by TEM and XDR in previous studies [5,19]. The same machine, process parameters and material have been used in the current study.

After a first single laser scan (Fig. 1a), the fusion zone border is barely visible but some small regions of crystalline particles can be seen in close proximity to the FZ. Here, existing nuclei had the possibility to grow during the thermal cycle. However, these clustered regions are few and one laser scan is not sufficient to cause significant crystallisation in the HAZ using the current process parameters. More particles forms after a second laser scan (Fig. 1b) and a banded region of crystalline particles become visible at the border of the FZ. Following the third laser scan (Fig. 1c), distinct regions containing crystalline particles are clearly present and circumvents the FZ, forming a clear crystalline HAZ. A magnified image of Fig. 1c is shown in Fig. 1d, in which the crystalline region at the FZ border is clearly visible. Fig. 1d shows that the HAZ following the third scan consists of zones of different characteristics. The HAZ closest to the FZ consists of larger particles (a few 100 nm) but at a lower particle number density. Further away from the FZ border (≈4–8 μm), the HAZ consists of even smaller particles at a higher cluster number density. The average number density of crystals in Fig. 1d is roughly estimated to be in the order of 10^{18} m^{-3}, using the Imagej software and by assuming a SEM penetration depth of 1 μm.

Selected parts of the HAZ were further studied by TEM, see Fig. 2a. From the bright field (BF) images (Fig. 2a-insets) a clear contrast between the amorphous matrix and the crystalline particles can be observed. This is further exemplified in the electron diffraction patterns obtained from a region with small crystals in Fig. 2b, where contributions from both the matrix (diffuse rings) and particles (diffraction spots) are observed. The high-resolution image in Fig. 2c shows the crystalline nature of the particles, further supported by the Fourier transform in Fig. 2d. All observed crystals were indexed by the CrysTBox toolbox to the Cu_2Zr_4O phase. These results are in line with previous investigations [5] and clearly shows that formation of crystals is mainly occurring in the HAZ.

The transition of particle characteristics in the HAZ indicates that the different regions experienced different thermal histories. In the region closest to the FZ, the material has been exposed to temperatures close to the melting point, where the growth rate is higher, hence the larger particle sizes. The higher particle number density in the HAZ, further away from the FZ, indicates that this region has been exposed to temperatures where the nucleation rate is dominating, which is known to occur at a lower temperature than the peak growth rate [15].

The FZ dimension was measured and estimated to ≈72–75 μm in width and ≈35–37 μm in depth. The shape is circular except from the inward curvature at the surface and a deeper "bump" at the bottom. The shape might be an effect of convective flow in the liquid and the whirlpool, which is visible in the SEM images, might involve chemical redistribution. However, detailed investigation of the fluid flow and composition in the melt pool is out of the scope of the present study.

4. Thermal modelling

A thermal FE model is developed to simulate the thermal field by multiple laser remelting of a single scan line. The model is developed in the commercial FE software MSC Marc for -solving the non-linear system of equations with full Newton–Raphson iterations. The modelling domain is limited to 1.0 × 1.0 × 0.5 mm (length, width, height) using eight-noded, three-dimensional brick elements. A local mesh refinement is applied in the proximity of the weld line, as shown in Fig. 3, and additional local mesh refinements are used in a control volume where the phase transformation model operates. This control volume is located at a position

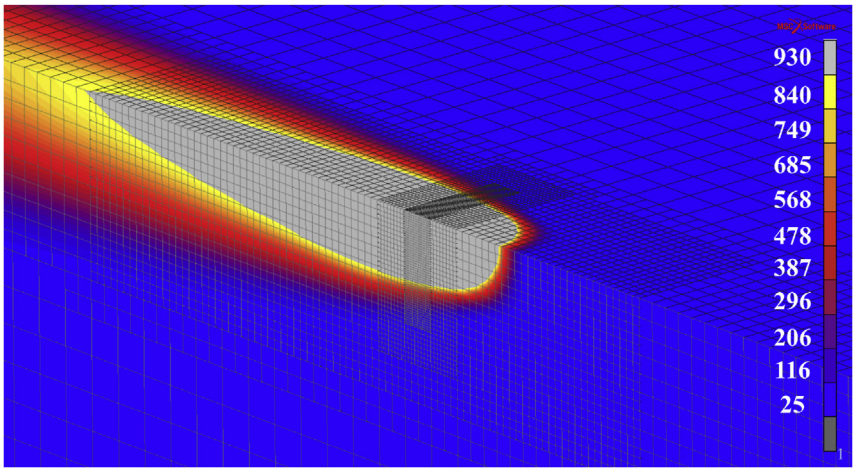

Fig. 3 – Thermal modelling domain (1.0 × 1.0 × 0.5 mm) with local mesh refinements in four levels. Colour contour shows temperature in °C.

where the melt pool is fully developed and steady-state condition is assumed. The side lengths of FEs in the control volume is 1.25 μm in all directions, as compared to the melt pool depth of ≈35 μm. The temperature is computed on all nodal positions and is interpolated to any position in the element using the shape function. The size of the elements also dictates the resolution of the phase transformation model as it is calculated at the integration points within the elements. The HAZ appears to be close to 7 μm by the SEM images in Fig. 1 and the chosen element size gives a spatial discretisation of about 1 μm in the phase transformation model.

4.1. *Heat source calibration*

Convective flow in the liquid will result in a relatively large melt pool as compared to the spot size of the concentrated laser power. The effective melt pool size can be related to the spatial energy density and is directly affected by the process parameters (energy input density), heat dissipation (material and environmental properties) and convective flow effects. Convective flow can be complex to simulate. Therefore, it is a good approach to approximate the heat source and model the effect of the distributed energy in the melt pool. In the current study, the heat source, q, is swept along the weld line at the scanning speed and is modelled with the well known three dimensional double ellipsoid with Gaussian distributed heat flux [20] as follows:

$$q = \frac{6\sqrt{3}\eta Q}{\pi\sqrt{\pi}c(h/2)^2}\exp\left(-\frac{3x'^2}{(h/2)^2}\right)\exp\left(-\frac{3y'^2}{(h/2)^2}\right)\exp\left(-\frac{3z'^2}{c^2}\right) \quad (1)$$

where Q is the laser power, η the laser efficiency, h the diameter of the numerical heat source and c the penetration depth. The variables x', y' and z' represents the local coordinates with origin in the center of the heat source, longitudinal, transverse and downward direction respectively. Parameters for the spatial heat distribution, material properties and energy absorption/laser efficiency was calibrated to fit the actual shape of the FZ determined on basis of the SEM images in Fig. 1. The heat input is controlled to ensure conservation of energy on the mesh grid.

The parameters h and c were selected to the smallest values of the fusion zone dimension observed be the third remelting scan, namely 35 and 70 μm. The laser efficiency, η was calibrated to provide a melt pool that fits the FZ dimensions observed by the experiments. A very good fit was achieved with $\eta = 0.35$ and this value was used during the following simulations. The resulting melt pool shape by the simulation is shown on top of the third scan SEM image in Fig. 4. A fixed temperature boundary condition of 25 °C is assigned to the bottom surface of the modelling domain. This enables the temperature to reach the initial state before the next scan is initiated without a build up of thermal energy.

A recent study by Grange et al. [21] presented a numerical expression for the laser power absorption, which provides a value of ~30% with current process parameters. In another

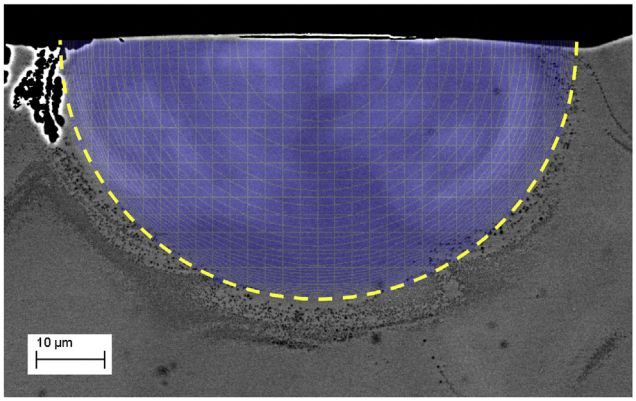

Fig. 4 – Simulated melt pool size on top of SEM image (third laser remelting). The fusion zone by the experiments is highlighted with the yellow dashed line.

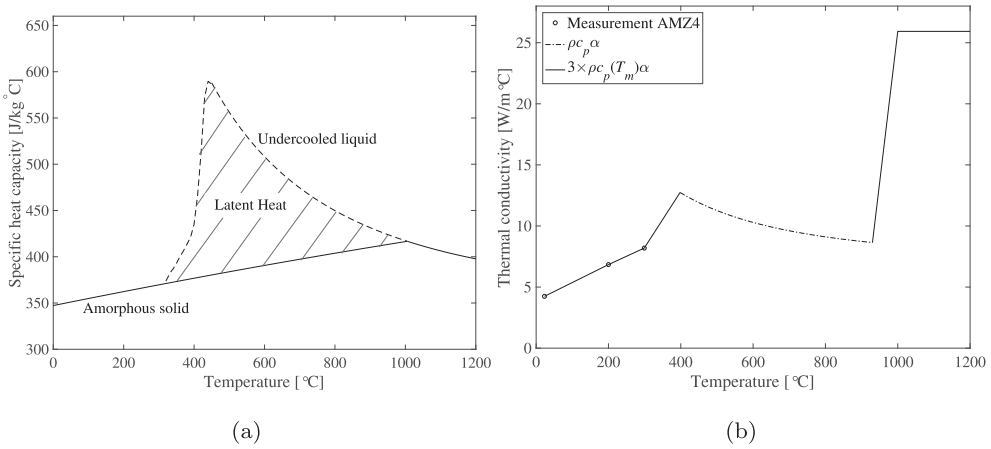

Fig. 5 – Material properties of AMZ4 used in the simulations. The specific heat capacity is represented by the solid line in (a). The latent heat by the glass transformation is computed by the area bounded by the highlighted curves. Thermal conductivity with marked measurement points and enhanced convective flow effects above the liquidus temperature (b).

study by Chiumenti et al. [22] they used a value of 45% which were in good agreement with experimental measurements. These studies were conducted on different alloys and with powder bed present, but are in the same range as our value of 35% efficiency. Shen et al. [23] found that at laser absorption coefficient of 13.6% gave similar results as compared to temperature measurements on the bottom surface of a 0.75 mm thick plate made of the $Zr_{52.5}Ti_5Al_{10}Ni_{14.6}Cu_{17.9}$ (at.%) alloy. The laser spot diameter was close to 11 times larger and the scan speed 1/4 of the values used in the current study and the heat source was modelled as a surface heat flux. This low value of η could not be used in the current study to match the melt pool dimension.

4.2. *Material data*

A material model of the specific heat capacity of amorphous AMZ4 was developed based on differential scanning calorimetry measurements by Heinrich et al. [24] during heating with 0.333 K/s. The heat capacity shows a sharp increase at the glass transition, $T_g = 671$ K as the amorphous phase relaxes into the undercooled liquid state, as shown in Fig. 5a. Modelling the sharp change in heat capacity by tabulated material data, as in previous work [25], requires high temporal resolution close to T_g in order to ensure that the effect of the changing heat capacity is included in the simulation. In the current study, the distinctive change in heat capacity in the undercooled liquid region is instead modelled using a latent heat of transformation, which is applied as a source term in the heat equation. It enables for the heat capacity to be modelled as a smooth curve shown as a base straight line, i.e., "Amorphous solid" in Fig. 5, throughout the undercooled liquid state and ensures that the effect of the glass transition is included. The latent heat is computed to 54 kJ/kg by evaluating the area enclosed by the two curves as highlighted in Fig. 5a.

The thermal diffusivity and conductivity of the material was measured at three different temperatures, see section 2.3, and the results are presented in Table 1. The model of thermal conductivity at temperatures below T_g is based on these measurements as shown in Fig. 5b. The thermal conductivity at temperatures above T_g is difficult to measure because of crystallisation and are estimated based on measurements of the thermal diffusivity and data for the specific heat by Heinrich et al. [24]. The conductivity is computed by $\rho c_p \alpha$, where ρ is the material density (assumed constant), c_p the temperature dependent heat capacity and α the thermal diffusivity, which is assumed constant above T_g [26]. The thermal diffusivity was measured to $\alpha = 2.79 \times 10^{-6}$ m^2/s at 299 °C (about 1% change from α at 200 °C) and is used to construct the thermal conductivity up to the melting temperature. The conductivity is scaled by a factor three above the liquidus temperature to mimic the effect of convective flow in the melt pool. Fig. 5b shows the complete curve of the thermal conductivity used in the simulations.

5. Phase modelling using classical nucleation and growth theory

The CNT provides a computational framework for describing the formation and growth of nuclei. The rate of nucleation and growth is derived based on a thermodynamic framework describing the required work of formation of a nucleus of critical size as well as the kinetic rate at which atoms attach/de-attach at the interface of the nucleus. The nucleation rate can be calculated numerically under transient conditions or approximated as steady-state nucleation. The resulting

Table 1 – Results of measured thermal properties of AMZ4.

Temperature [°C]	Thermal conductivity [W/mK]	Thermal diffusivity [$\times 10^{-6}$ m/s]
23	4.25	2.066
200	6.84	2.82
299	8.19	2.79

equations requires material-specific parameters such as the change in Gibbs energy, interfacial energy, and diffusivity as a function of temperature. The CNT model used in the present study has been adapted to AMZ4 by utilizing measured thermodynamic and kinetic quantities available in the literature [24,27], as well as calibration to a measured time–temperature-transformation (TTT) diagram over the full temperature range [15]. Note that the model does not discriminate between phases of different crystalline structures. The change in Gibbs energy is estimated from measurements of the specific heat capacity of the liquid and crystalline state consisting of multiple crystalline phases. For in-depth details of the model description and calibration, the reader is referred to [15].

5.1. Nucleation

According to classic nucleation theory, the evolution of the time-dependent cluster size distribution $N(n, t)$, defined as the number of clusters of size n and time t per unit volume, can be described by a set of coupled ordinary differential equations of the form [28,29]:

$$\frac{\partial N(n,t)}{\partial t} = N(n-1,t)k^{+}(n-1) - N(n,t)(k^{+}(n)+k^{-}(n)) + N(n+1,t)k^{-}(n+1) \quad (2)$$

where n is the number of atoms in the cluster, $k^{+}(n)$ and $k^{-}(n)$ is the attachment and de-attachment rates of single atoms to a cluster of size n per unit time, respectively. Based on Eq. (2), the number of clusters that form of size n at time t (number of clusters per unit volume and time), i.e. the nucleation rate $I(n, t)$, is defined as [28,29]:

$$I(n,t) = N(n,t)k^{+}(n) - N(n+1)k^{-}(n+1). \quad (3)$$

The rate of atomic attachment and de-attachment to a cluster of spherical shape is estimated using transition state theory to provide [30]:

$$k^{+}(n) = \frac{24n^{2/3}D}{\lambda^2}\exp\left(-\frac{\delta G(n)}{2k_B T}\right)$$
$$k^{-}(n) = \frac{24n^{2/3}D}{\lambda^2}\exp\left(+\frac{\delta G(n)}{2k_B T}\right) \quad (4)$$

where D is the effective diffusivity and λ is the atomic jump distance in the matrix phase, k_B is the Boltzmann constant and T is the absolute temperature. As seen in Eq. (4), the rate at which atoms attach or de-attach at the interface depends on the change in Gibbs energy between the two cluster sizes, $\delta G(n) = \Delta G(n+1) - \Delta G(n)$, where $\Delta G(n)$ is the energy required to form a cluster of size n, defined as:

$$\Delta G(n) = n\Delta G' + (36\pi)^{1/3}\bar{v}^{2/3}n^{2/3}\sigma \quad (5)$$

where $\bar{v}$ is the average atomic volume. Eq. (5) describes an energetic competition between the release of bulk Gibbs energy per atom $\Delta G' < 0$ and the energy required to form the interface per unit area $\sigma > 0$ between the two phases. Hence, there exists a critical size $n^{*} = 32\pi\bar{v}^2\sigma^3/3|\Delta G'|^3$ at which the change in Gibbs energy possesses a maximum value where clusters smaller than n^{*} have a higher probability to dissolve ($k^{-}(n) > k^{+}(n)$), while clusters larger than n^{*} have a higher probability to grow to macroscopic sizes ($k^{+}(n) > k^{-}(n)$).

The differential equations in Eq. (2) dictate the growth and dissolution of clusters in a general format, allowing for the nucleation rate $I(n, t)$ to vary with time, depending on the evolution of the cluster size distribution. However, often a steady-state condition is assumed, meaning that the cluster size distribution evolves instantaneously to the steady-state cluster size distribution at each temperature, and that the nucleation rate is independent of time. The steady-state nucleation rate is usually expressed as [28,29,31]:

$$I^{st} = N_0 Z k^{+}(n^{*})\exp\left(-\frac{\Delta G(n^{*})}{k_B T}\right) \quad (6)$$

where N_0 is the number of atoms per unit volume in the system, $Z = (|\Delta G'|/6\pi k_B T n^{*})^{1/2}$ is the Zeldovich factor, $k^{+}(n^{*})$ and $\Delta G(n^{*})$ are the atomic attachment rate and change in Gibbs energy evaluated at the critical size, respectively.

Numerical solutions of Eq. (2) have been shown to deviate from the steady-state assumption of nucleation under rapid cooling or heating [28,29,32]. Due to the high heating and cooling rates associated with the PBF-LB process, it is therefore expected that the transient nucleation effects can be significant [15]. We therefore apply and compare the two different models for nucleation: the numerical solution of transient nucleation obtained by solving Eq. (2), as well as the analytical solution of steady-state nucleation given by Eq. (6). The set of ordinary differential equations given by Eq. (2) are stiff and requires significantly more computational resources in comparison to the analytical expression of steady-state nucleation. Hence, the solution procedure of the two models is differentiated and the transient model is solved externally using the temperature history as input, while the steady-state model is solved in a coupled staggered approach with the thermal FE model.

5.2. Growth of supercritical clusters

The number of nuclei per unit volume $\widehat{N}_i$ that forms during a time increment i is calculated by integration of the nucleation rate with respect to time, i.e. by numerical evaluation of:

$$\widehat{N}_i = \int_{t_{i-1}}^{t_i} I_i(n_{eval}, t')dt' \quad (7)$$

using the trapezoidal rule. Here n_{eval} denotes the size at which nuclei are assumed to grow, t_{i-1} and t_i are the times prior to and after the time increment i, respectively. Written in terms of the cluster radius r, this value is chosen to be $r_{eval} = r^{*}_{T_{max}} + 0.5(k_B T_{max}/\pi\sigma)^{1/2}$, where $r^{*}_{T_{max}}$ is the critical size evaluated at the maximum temperature T_{max} of the simulation. Assuming spherical particles, $n = 4\pi r^3/3\bar{v}$ for any given cluster radius r.

The growth of clusters is computed using a Lagrange-like approach [31], in which the number density of supercritical clusters are stored in an array. The array is updated at each time step, first by adding new clusters using Eq. (7), following growth in which the size of the clusters is updated. The

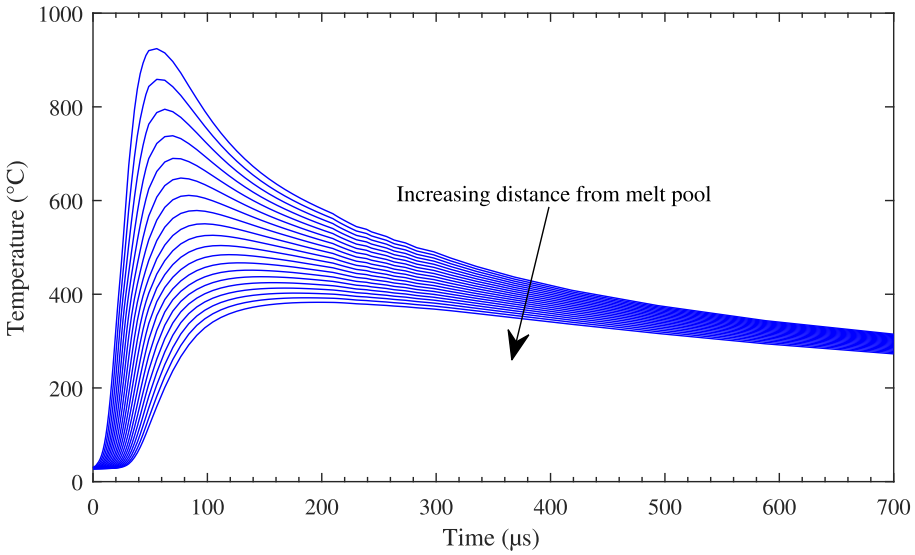

Fig. 6 – Predicted temperature history in the first 20 μm from the FZ at the bottom of the melt pool. The temperature is sampled in steps of 1 μm in increasing distance from the FZ.

growth is calculated using an explicit time-stepping scheme given by:

$$r(t_i) = r(t_{i-1}) + u(r(t_{i-1}))\Delta t \tag{8}$$

where Δt is the time step and $u(r)$ is the size-dependent growth rate. In the present work, polymorphic growth is assumed and the growth rate is taken as [28,33]:

$$u(r) = \frac{16D}{\lambda^2}\left(\frac{3\bar{v}}{4\pi}\right)^{1/3}\sinh\left[\frac{\bar{v}}{2k_BT}\left(|\Delta G_v| - \frac{2\sigma}{r}\right)\right] \tag{9}$$

where ΔG_v is the bulk Gibbs energy release per unit volume. In order to avoid numerical issues, all dissolving clusters with a radius smaller than $r^*/5$ are removed from the size distribution.

The crystalline volume fraction is computed at the end of each time step using the Johnson-Mehl-Avrami-Kolmogorov (JMAK) equation [34], given by:

$$x(t) = 1 - \exp(-x^{ext}) \tag{10}$$

where x^{ext} is the extended volume fraction. For a non-isothermal process discretised in time, the extended volume fraction can be computed using $x^{ext} = 4\pi/3\sum N_i r_i^3$ [35]. Where N_i is the number density of clusters formed during time increment i and r_i is the radius of the corresponding clusters. As previously described, these quantities are available from the array stored throughout the simulation.

5.3. *Coupling with thermal FE model*

The steady-state CNT model is implemented in the FE model and solved for at all integration points in the control volume described in section 4. The model is "one-way coupled" meaning that the phase transformation is computed after each converged time increment by the thermal model. The thermal solver uses an implicit approach and an adaptive time-stepping scheme and can therefore use relatively large time increments and still satisfy the convergence criteria for the temperature. Because of the different characteristic time scales of the thermal model and the CNT model, the nucleation and growth are solved in sub-steps using a Lagrangian approach within the time/temperature increment of the FE model. The increment of a sub-step is defined by the ratio of the critical nuclei radius, $r^*(T)$ at the beginning, ${}^jT$ and the end temperature ${}^{j+1}T$ of the sub-step, as proposed in [28] (sub-step increments denoted j). The ratio was chosen to not differ more than one percent, i.e., $|r^*({}^jT)/r^*({}^{j+1}T+1) - 1| < 1\%$. Furthermore, the number of nuclei formed during a sub-step, ${}^jN$, is computed using the steady-state nucleation rate, by Eq. (7) with the mean temperature and time increment of the sub-step. To ensure a good approximation, a second condition is included by computing the accumulative nucleated clusters ${}^jN_{acc}$ by an additional splitting of the sub-step. The relative difference between the previous (${}^jN$) and current (${}^jN_{acc}$) solution was chosen not to be greater than 0.1%: $|{}^jN - {}^jN_{acc}|/{}^jN < 0.1\%$. Thus, the temperature ${}^{j+1}T$, dictating the size of the sub-step, was chosen by linear interpolation within the time/temperature increment of the FE model, such that both conditions were satisfied. The phase transformation model can therefore be used with confidence regardless of the time increment used by the thermal solution.

6. Simulation of phase evolution by multiple laser scanning

The crystalline phase evolution was computed during the thermal simulation at all integration points in the control volume. Each scan resulted in nucleation and growth of crystalline clusters and the crystalline volume fraction,

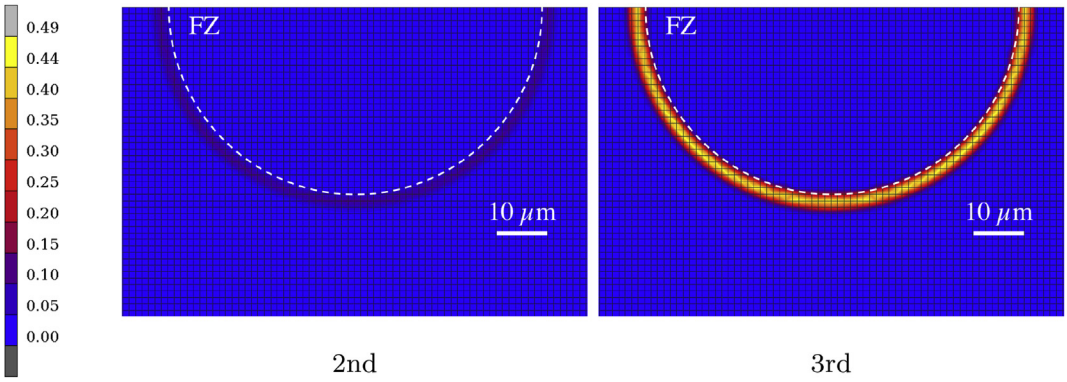

Fig. 7 – Contour plots showing the distribution of crystalline volume fraction in the HAZ after two and three scans. Mesh grid size is 1.25 μm and the legend shows the nodal average defined from the third scan.

number density, and mean radius were enabled for post-processing. The time between each scan was long enough for the material to reach ambient temperature without any accumulation of thermal energy. The temperature history in the first 20 μm along the radial distance from the FZ in steps of 1 μm is shown Fig. 6.

6.1. *Crystalline volume fraction*

The crystalline volume fraction by steady-state nucleation was computed and compared to observations from the experiments. Fig. 7 shows the simulated crystalline phase evolution during the melting cycles in a cross-section perpendicular to the scanning direction. The contour plots shows the crystalline volume fraction after the second and third scan with the legend of the third scan. With the chosen limits, it is not possible to detect any crystalline volume fraction from the first scan. Clusters that formed during the first scan were never exposed to high temperatures where growth dominates the phase transformation. However, after the second scan, a band of a crystalline structure became visible in the HAZ, with a maximum volume fraction of 9%. As a result, clusters formed in the HAZ from the first scan were exposed to high temperatures and could grow to macroscopic sizes. The crystalline volume fraction continued to increase significantly during the third scan to reach a peak value of about 49%. The resulting crystalline volume fraction, mean radius, and number density after each scan is presented in Table 2.

6.2. *Number density*

The number density increased with 3.33×10^{16} m^{-3} after each scan during the simulation. The consistency is expected since each scan results in identical thermal history and nucleation rate. The distribution, as seen in Fig. 8, shows that the highest number density is located approximately 15–20 μm from the FZ, in the low-temperature region of the HAZ. In this region of the HAZ, the temperature was mostly in the regime where the steady-state nucleation rate is the highest [15].

6.3. *Mean cluster radius*

The mean cluster radius is computed during the simulation and the distribution after the third scan is presented in Fig. 9. The results clearly show that larger clusters are concentrated close to the FZ. This is a result of the growth rate given by Eq. (9), which obtain its highest value at temperatures close to the melting point. The cluster sizes were smaller further away in the HAZ due to the lower growth rate at the lower temperatures. The mean radius a few micrometers out in the HAZ is also estimated to be in the same order of magnitude as in the remelted material. The smallest mean clusters radius are, according to the legend in Fig. 9, at least a factor ten smaller than the largest mean cluster radius.

6.4. *Transient nucleation*

Fig. 10 shows the calculated crystalline volume fraction along the distance from the FZ using the transient model together with results from the steady-state nucleation model. The peak fraction after three scans reached 0.047% at the closest distance from the FZ. The corresponding value by steady-state nucleation is close to 60%.

The number density along the radial distance from the FZ after each scan is presented in Fig. 11. The number density gradually increase along the HAZ from approximately 1×10^{16} to 9×10^{16} m^{-3} by the steady-state nucleation model in similar

Table 2 – Simulation results of phase evolution by multiple melting of a single-track. The values represents the maximum value of all nodes of the FE-model using nodal averaging.

Scan	Maximum crystalline volume fraction [%]	Maximum clusters number density [m^{-3}]	Maximum mean cluster radius [nm]
1	0.12	3.33×10^{16}	13.9
2	9.06	6.68×10^{16}	431
3	49.4	1.00×10^{17}	850

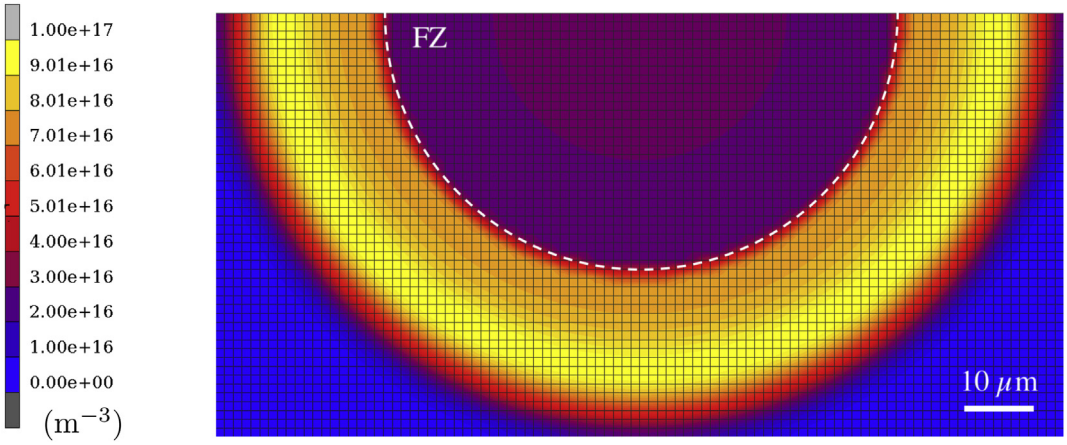

Fig. 8 – Number density of precipitates after third scan.

manner as shown in Fig. 8. By the transient nucleation model, a peak value of about 2×10^{13} m^{-3} became visible at around 7 μm from the FZ.

The computed mean cluster radius after each scan is presented in Fig. 12. Both models predict a decreasing mean cluster radius along the distance from the FZ. The transient nucleation model predicts larger cluster sizes on the average, as compared to the steady-state nucleation assumption. This result is a consequence of the difference in nucleation rate between the two models, in which the steady-state assumption results in a larger amount of nano-sized crystals because of the peak nucleation rate at low temperatures where the material spends a relatively long time.

7. Discussion

The phase transformation model coupled with the thermal FE model demonstrates a direct correlation between successive laser melting and formation of crystalline precipitates. We compare the trend from the simulation to quantitative observations from the experiments. It is observed, by simulation and SEM imaging in Fig. 1, that the crystalline volume fraction in the HAZ increases with the total energy input. The simulated phase evolution assuming steady-state nucleation correlates well with the observed trend in increasing crystallisation for each laser pass by the SEM images. A small amount of crystallisation is present after two laser passes and a major crystallisation occurs following the third laser pass. Similar trends can be seen in the experimental studies in [7,8], where crystallisation increase with additional remelting, yet appears clearly after close to twenty remelting cycles. However, these studies were performed on alloy $Zr_{55}Cu_{30}Al_{10}Ni_5$ with significantly different process parameters and amorphous initial state.

The temperature history of a single scan shown in Fig. 6 can explain the gradient of cluster size and number density in the HAZ. High-temperature locations will experience high growth rates and clusters can therefore grow to larger sizes. Thus, the largest clusters are found close to the fusion zone and the size decreases with the distance from the melt pool. Further away from the FZ, the material is subjected to lower temperatures for a longer duration at which the nucleation rate is higher. Hence, the resulting number density becomes higher at a certain distance from the FZ.

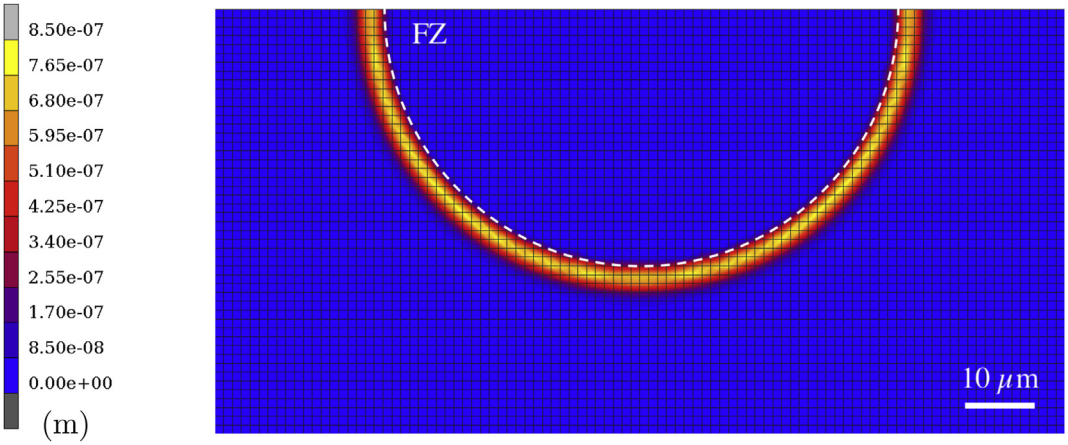

Fig. 9 – Mean cluster radius of the precipitates after the third scan.

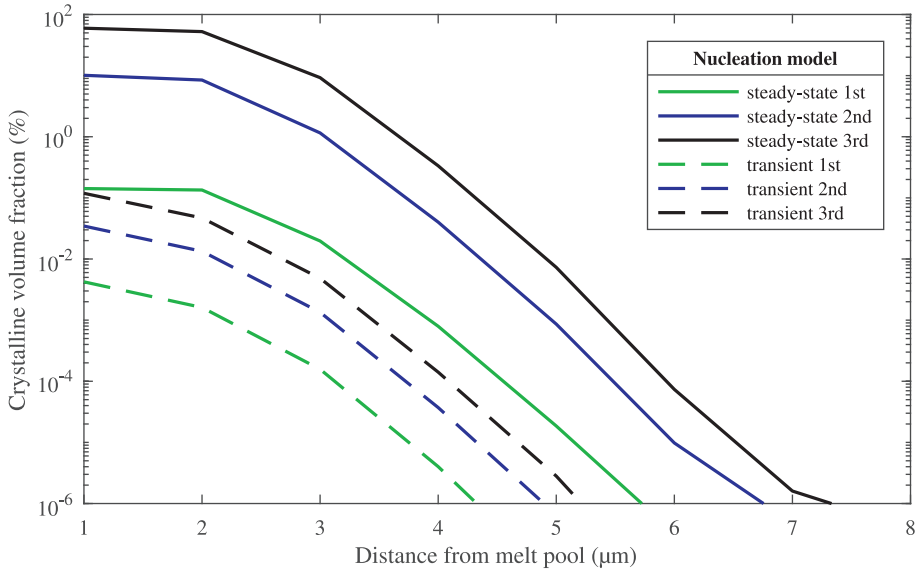

Fig. 10 – Crystalline volume fraction after 1–3 scans with regard to steady-state (solid lines) and transient nucleation (dashed lines) respectively. The line colour green-blue-black represent laser melting scans 1-2-3 times respectively.

The width of the HAZ is another metric that can be used to compare the results. The width of the HAZ is approximately 9 μm in the SEM image following the third laser pass (Fig. 1c). However, variations in width depending on location can be seen and in the upper right side, it is as low as 3 μm. The width of the HAZ is also likely to vary in the scanning direction because of small variations in laser and material interaction. The variation of the width of the HAZ is not captured in the simulations, partly because of the simplified heat input model that does not consider the convective flow, and partly because of ignoring heat loss by radiation and convection on the surface. However, if we define the HAZ as the zone with a crystalline volume fraction >0.01%, the width of the HAZ becomes 5 μm for the steady-state model and 3 μm for the transient model after the third laser pass (see Fig. 10), which is of comparable magnitude relative the experimental observation in Fig. 1c. This indicates that the model can predict the width of the HAZ within reasonable accuracy and on a relevant length scale with process parameters used in the PBF-LB process.

In section 3, the average number density of crystals after the third scan was roughly estimated to be in the order of 10^{18} m^{-3}. This number is one to two orders of magnitude higher than the prediction by the steady-state model and several orders of magnitude higher than the transient model as shown in Fig. 11. The estimated value is further assumed to be even higher because of all nano-sized clusters that were undetected and that the number density is evaluated using the cross-section area. One explanation for the excess of clusters by the experiments is the thermal history of the substrate from manufacturing. The substrates are made by PBF-LB in which multiple reheating is inevitable. Thus, they are not completely free from crystals and some crystalline regions can be seen in the SEM images in Fig. 1. It should be noted that other experimental techniques, such as small-angle scattering would provide a different experimental result since it probes the sample on a different length-scale and over a larger volume [5,36].

The comparison shows that both models under-predict the nucleation rate. This could be a result of the assumptions invoved in calibrating the model to DSC experiments [15]. For example, a constant growth rate using the limit of Eq. (9) was assumed. This equation is only valid for a polymorphic transformation in which the composition of the crystal and matrix is equal. The electron diffraction pattern in Fig. 2 shows that oxygen-enriched Cu_2Zr_4O crystals form in the HAZ. The growth of this phase involves chemical redistribution at the interface which results in a time-dependent growth rate controlled by long-range diffusion. Hence it is likely that Eq. (9) overestimates the growth rate. This observation is also in agreement with the predicted mean cluster radius in Fig. 12 and Table 2 which is larger than the particles observed in the SEM images. Since the volume fraction scale by r^3 but is proportional to N (see Eq. (10)), a lower growth rate would result in a higher nucleation rate to obtain the same crystalline volume fraction. Thus, the actual nucleation rate is likely to be of higher magnitude than predicted by the models. Quite recently, corrections to Eq. (5) for small cluster sizes have shown to result in an increased nucleation rate [37]. Such improvements together with the development of a diffusion-controlled growth model could be a direction for further development.

Although the nucleation rate is under-predicted by the current implementation, the results are qualitatively correct. A clear tendency for crystallisation is observed in the HAZ, with a gradient in cluster size and number density. In the case of the transient model, a sharp peak in number density is observed a few micrometers from the fusion zone, comparable to the observations by the experiments. By comparing with the thermal history in Fig. 6, this indicates that the peak nucleation rate should occur around 550–700 °C for the present material and thermal conditions, which is in good agreement with the peak nucleation rate of the transient model at 620 °C. The large deviation from the steady-state

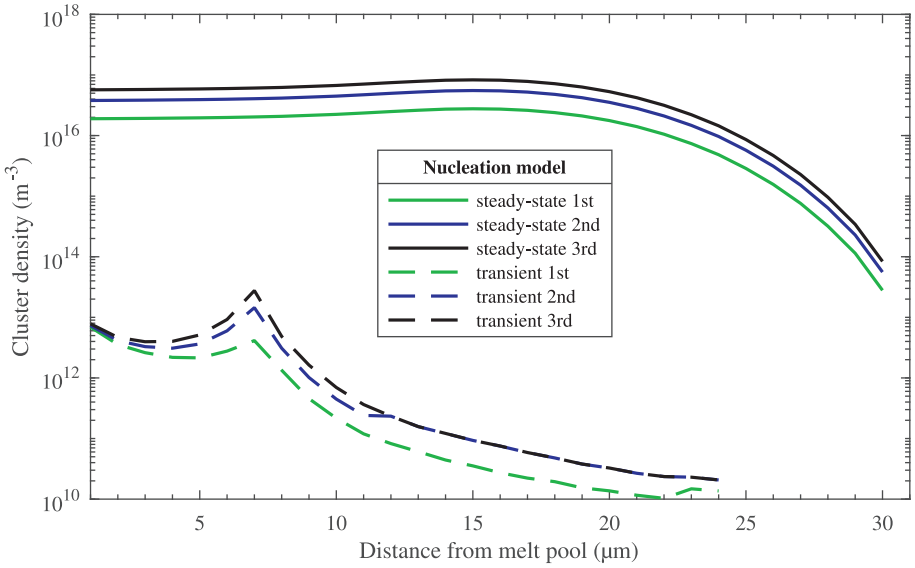

Fig. 11 – Custer density after 1–3 scans with regard to steady-state (solid lines) and transient nucleation (dashed lines) respectively. The line colour green-blue-black represent laser melting scans 1-2-3 times respectively.

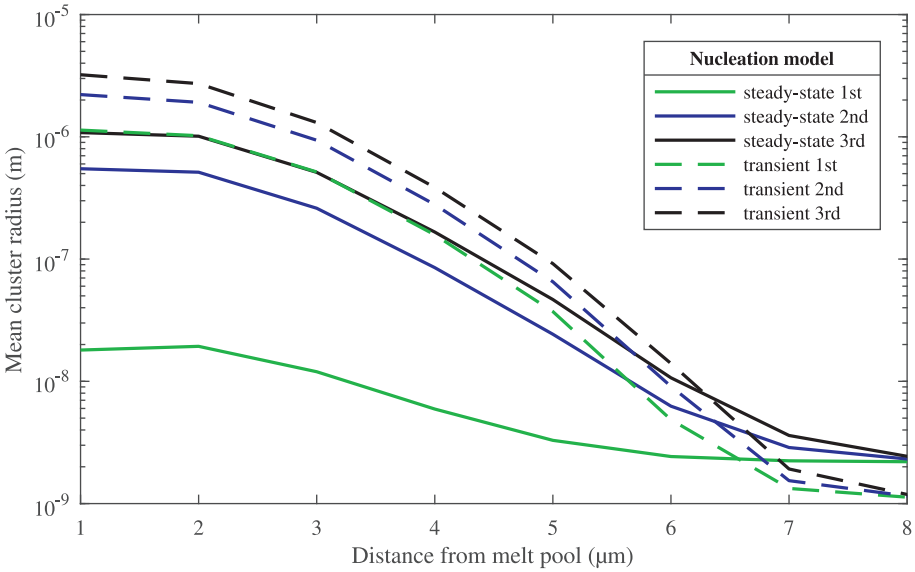

Fig. 12 – Mean cluster radius after 1–3 scans with regard to steady-state (solid lines) and transient nucleation (dashed lines) respectively. The line colour green-blue-black represent laser melting scans 1-2-3 times respectively.

nucleation indicates that these effects can be prominent under the rapid heating and cooling in PBF-LB, in good correlation with our previous results [15]. The results from the simulations in the present study show that thermal simulations coupled with a CNT model can be a promising tool for predicting the crystallisation rate of BMGs during PBF-LB.

8. Conclusion

A phase transformation model for steady-state nucleation has been implemented in a thermal FE model to simulate the evolution of the crystalline phase in the metallic glass alloy AMZ4 during multiple laser remelting. The model should be valid for any glass-forming alloy that crystallises through nucleation and growth in a polymorphic manner. A decoupled model for transient nucleation was also used and both models have been compared with experimental results using multiple laser remelting on a single string. Both simulation and experimental work show that multiple reheating cycles results in formation of crystals in the HAZ and variations in crystal size and number density are observed. Simulation of the relative increase in crystalline volume fraction after each scan is of comparable magnitude to experiments. The model is also capable of predicting the size of the HAZ on a comparable length scale to that of the experiments with

process parameters used in PBF-LB. A model such as this can be a useful tool when developing process parameters for PBF-LB to reduce the formation of undesirable crystalline structures. Multiple reheating by overlapping HAZ should be minimized to reduce the amount of crystallisation by growth of existing nuclei.

Declaration of Competing Interest

The authors declare that they have no known competing financial interests or personal relationships that could have appeared to influence the work reported in this paper.

Acknowledgment

This research was supported by the Swedish Foundation for Strategic Research, SSF, project 'Development of Process and Material in Additive Manufacturing', Reference number GMT14-0048.

REFERENCES

[1] Suryanarayana C, Inoue A. Bulk metallic glasses. CRC Press; 2011.
[2] Williams E, Lavery N. Laser processing of bulk metallic glass: a review. J Mater Process Technol 2017;247(March):73–91. https://doi.org/10.1016/j.jmatprotec.2017.03.034.
[3] Liu H, Jiang Q, Huo J, Zhang Y, Yang W, Li X. Crystallization in additive manufacturing of metallic glasses: a review. Additive Manufacturing 2020;36(September):101568. https://doi.org/10.1016/j.addma.2020.101568.
[4] Jung HY, Choi SJ, Prashanth KG, Stoica M, Scudino S, Yi S, et al. Fabrication of Fe-based bulk metallic glass by selective laser melting: a parameter study. Mater Des 2015;86:703–8. https://doi.org/10.1016/j.matdes.2015.07.145.
[5] Marattukalam JJ, Pacheco V, Karlsson D, Riekehr L, Lindwall J, Forsberg F, et al. Development of process parameters for selective laser melting of a zr-based bulk metallic glass. Additive Manufacturing 2020;33:101124. https://doi.org/10.1016/j.addma.2020.101124.
[6] Li X, Roberts M, O'Keeffe S, Sercombe T. Selective laser melting of Zr-based bulk metallic glasses: processing, microstructure and mechanical properties. Mater Des 2016;112:217–26. https://doi.org/10.1016/j.matdes.2016.09.071.
[7] Yang G, Lin X, Liu F, Hu Q, Ma L, Li J, et al. Laser solid forming Zr-based bulk metallic glass. Intermetallics 2012;22:110–5. https://doi.org/10.1016/j.intermet.2011.10.008.
[8] Zhang Y, Lin X, Wang L, Wei L, Liu F, Huang W. Microstructural analysis of $Zr_{55}Cu_{30}A_{10}Ni_5$ bulk metallic glasses by laser surface remelting and laser solid forming. Intermetallics 2015;66:22–30. https://doi.org/10.1016/j.intermet.2015.06.007.
[9] Oliveira J, Santos T, Miranda R. Revisiting fundamental welding concepts to improve additive manufacturing: from theory to practice. Prog Mater Sci 2020;107:100590. https://doi.org/10.1016/j.pmatsci.2019.100590.
[10] Shen YT, Kim TH, Gangopadhyay AK, Kelton KF. Icosahedral order, frustration, and the glass transition: evidence from time-dependent nucleation and supercooled liquid structure studies. Phys Rev Lett 2009;102(5):6–9. https://doi.org/10.1103/PhysRevLett.102.057801.
[11] Pogatscher S, Uggowitzer PJ, Löffler JF. In-situ probing of metallic glass formation and crystallization upon heating and cooling via fast differential scanning calorimetry. Appl Phys Lett 2014;104(25):251908. https://doi.org/10.1063/1.4884940.
[12] Kosiba K, Scudino S, Kobold R, Kühn U, Greer AL, Eckert J, et al. Transient nucleation and microstructural design in flash-annealed bulk metallic glasses. Acta Mater 2017;127:416–25. https://doi.org/10.1016/j.actamat.2017.01.059.
[13] Fisk M, Lundbäck A, Edberg J, Zhou JM. Simulation of microstructural evolution during repair welding of an IN718 plate. Finite Elem Anal Des 2016;120:92–101. https://doi.org/10.1016/j.finel.2016.07.007.
[14] Shen Y, Li Y, Tsai H-L. Evolution of crystalline phase during laser processing of Zr-based metallic glass. J Non-Cryst Solids 2018;481:299–305. https://doi.org/10.1016/J.JNONCRYSOL.2017.11.001.
[15] Ericsson A, Pacheco V, Sahlberg M, Lindwall J, Hallberg H, Fisk M. Transient nucleation in selective laser melting of zr-based bulk metallic glass. Mater Des 2020;195:108958. https://doi.org/10.1016/j.matdes.2020.108958.
[16] Heraeus. Data sheet amloy-zr01. URL, https://www.heraeus.com/media/media/group/media_group/products/amorphous_metals/datasheets_1/Datasheet_Layout_AMLOY-ZR01.pdf.
[17] https://images-eu.ssl-images-amazon.com/images/I/919nxYIEJIS.pdf.
[18] Klinger M. Crystbox - crystallographic toolbox. Prague: Institute of Physics of the Czech Academy of Sciences; 2015, ISBN 978-80-905962-3-8. URL, http://www.fzu.cz/klinger/crystbox.pdf.
[19] Pacheco V, Karlsson D, Marattukalam JJ, Stolpe M, Hjörvarsson B, Jansson U, et al. Thermal stability and crystallization of a Zr-based metallic glass produced by suction casting and selective laser melting. J Alloys Compd 2020;825:153995. https://doi.org/10.1016/j.jallcom.2020.153995.
[20] Goldak J, Chakravarti A, Bibby M. A new finite element model for welding heat sources. Metall Trans A B 1984;15(2):299–305. https://doi.org/10.1007/BF02667333.
[21] Grange D, Queva A, Guillemot G, Bellet M, Bartout J-D, Colin C. Effect of processing parameters during the laser beam melting of Inconel 738: comparison between simulated and experimental melt pool shape. J Mater Process Technol 2021;289:116897. https://doi.org/10.1016/J.JMATPROTEC.2020.116897.
[22] Chiumenti M, Neiva E, Salsi E, Cervera M, Badia S, Moya J, et al. Numerical modelling and experimental validation in selective laser melting. Additive Manufacturing 2017;18:171–85. https://doi.org/10.1016/J.ADDMA.2017.09.002.
[23] Shen Y, Li Y, Chen C, Tsai HL. 3D printing of large, complex metallic glass structures. Mater Des 2017;117:213–22. https://doi.org/10.1016/j.matdes.2016.12.087.
[24] Heinrich J, Busch R, Nonnenmacher B. Processing of a bulk metallic glass forming alloy based on industrial grade Zr. Intermetallics 2012;25:1–4. https://doi.org/10.1016/j.intermet.2012.02.011.
[25] Lindwall J, Pacheco V, Sahlberg M, Lundbäck A, Lindgren L-E. Thermal simulation and phase modeling of bulk metallic glass in the powder bed fusion process. Additive Manufacturing 2019;27:345–52. https://doi.org/10.1016/j.addma.2019.03.011.
[26] Yamasaki M, Kagao S, Kawamura Y. Thermal diffusivity and conductivity of Zr55Al10Ni5Cu30 bulk metallic glass. Scripta

Mater 2005;53(1):63–7. https://doi.org/10.1016/j.scriptamat.2005.03.021.
[27] Hembree W. High temperature rheology of Zr-based bulk metallic glass forming liquids. Doctorial thesis. Universität des Saarlandes; 2015.
[28] Kelton KF, Greer A. Transient nucleation effects in glass formation. J Non-Cryst Solids 1986;79:295–309. https://doi.org/10.1016/0022-3093(86)90229-2.
[29] Kelton KF. Numerical model for isothermal and non-isothermal crystallization of liquids and glasses. J Non-Cryst Solids 1993;163(3):283–96. https://doi.org/10.1016/0022-3093(93)91306-N.
[30] Wu DT. Nucleation theory. In: Ehrenreich F, Spaepen H, editors. Solid state physics - advances in research and applications, vol. 50. Academic Press; 1997. p. 37–187. https://doi.org/10.1016/S0081-1947(08)60604-9.
[31] Perez M, Dumont M, Acevedo-Reyes D. Implementation of classical nucleation and growth theories for precipitation. Acta Mater 2008;56(9):2119–32. https://doi.org/10.1016/j.actamat.2007.12.050.
[32] Li HQ, Yan JH, Xu JG, Li HQ, Yan JH, Xu JG. Calculation of transient nucleation rate for Pd and Zr based metallic glass alloys. Mater Sci Technol 2009;25(7):935–8. https://doi.org/10.1179/174328408X365739.
[33] Gránásy L. Quantitative analysis of the classical nucleation theory on glass- forming alloys. J Non-Cryst Solids 1993;158:514–8. https://doi.org/10.1016/0022-3093(93)90010-U.
[34] Fanfoni M, Tomellini M. The johnson-mehl- avrami-kohnogorov model: a brief review. Il Nuovo Cimento D 1998;20(7):1171–82. https://doi.org/10.1007/BF03185527.
[35] Kelton K. Transient nucleation in glasses. Mater Sci Eng, B 1995;32(3):145–51. https://doi.org/10.1016/0921-5107(95)80023-9. containing papers presented at the Indo-US Workshop on Nucleation and Growth in Solids.
[36] Ericsson A, Pacheco V, Marattukalam J, Dalgliesh R, Rennie A, Fisk M, et al. Crystallization of a zr-based metallic glass produced by laser powder bed fusion and suction casting. J Non-Cryst Solids 2021;571:120891. https://doi.org/10.1016/j.jnoncrysol.2021.120891.
[37] Abyzov AS, Schmelzer JWP, Fokin VM, Zanotto ED. Crystallization of supercooled liquids: self-consistency correction of the steady-state nucleation rate. Entropy 2020;22(5). https://doi.org/10.3390/e22050558.